Supporting Information

for

Boosting OER via Metal-Support Interaction and H-Bond Network: Amorphous RuO_x on Fluorinated Ruddlesden-Popper Perovskite

*Ziye Feng[a], Zijie Peng[a], Yang Xu[b], Ming Zhang[c, d], Junfang Cheng[a]**

[a]SJTU Paris Elite Institute of Technology, Shanghai Jiao Tong University, Shanghai 200240, China

[b]School of Mechanical Engineering, Shanghai Jiao Tong University, Shanghai 200240, China

[c]CAS Key Laboratory of Design and Assembly of Functional Nanostructures, and Fujian Key Laboratory of Nanomaterials, Fujian Institute of Research on the Structure of Matter, Chinese Academy of Sciences, Fuzhou 350002, China

[d]Xiamen Key Laboratory of Rare Earth Photoelectric Functional Materials, Xiamen Institute of Rare Earth Materials, Haixi Institutes, Chinese Academy of Sciences, Xiamen 361021, China

***E-mail**: chengjunfang@sjtu.edu.cn

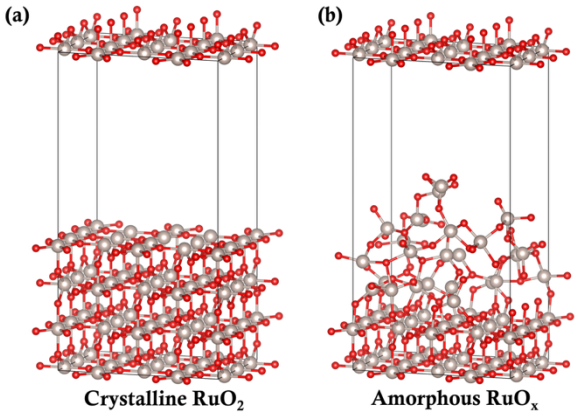

Figure S1. Optimized atomic models of (a) crystalline RuO_2 and (b) amorphous RuO_x; gray spheres denote Ru atoms, and red spheres denote O atoms.

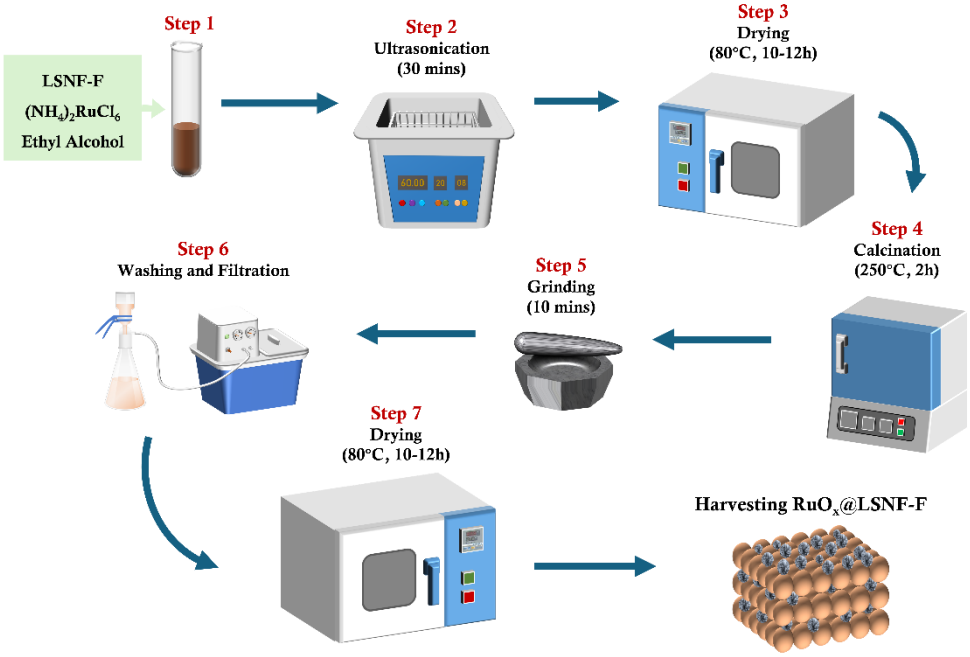

Figure S2. Schematic diagram of the synthesis process of RuO_x@LSNF-F.

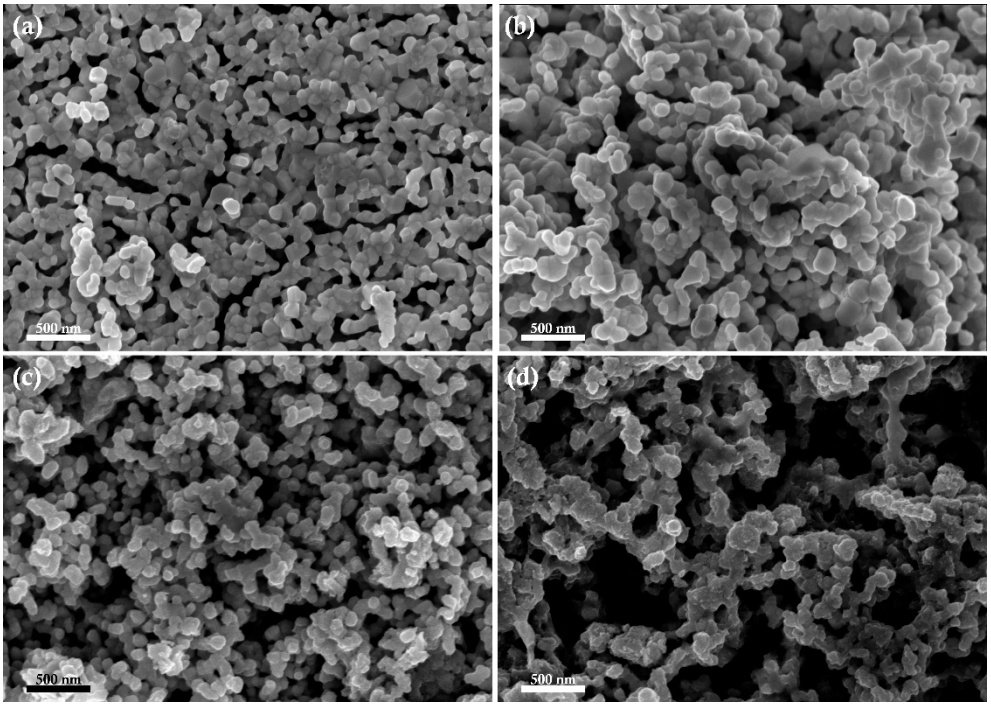

Figure S3. SEM image of (a) LSNF; (b) LSNF-F; (c) RuO_x@LSNF; (d) RuO_x@LSNF-F.

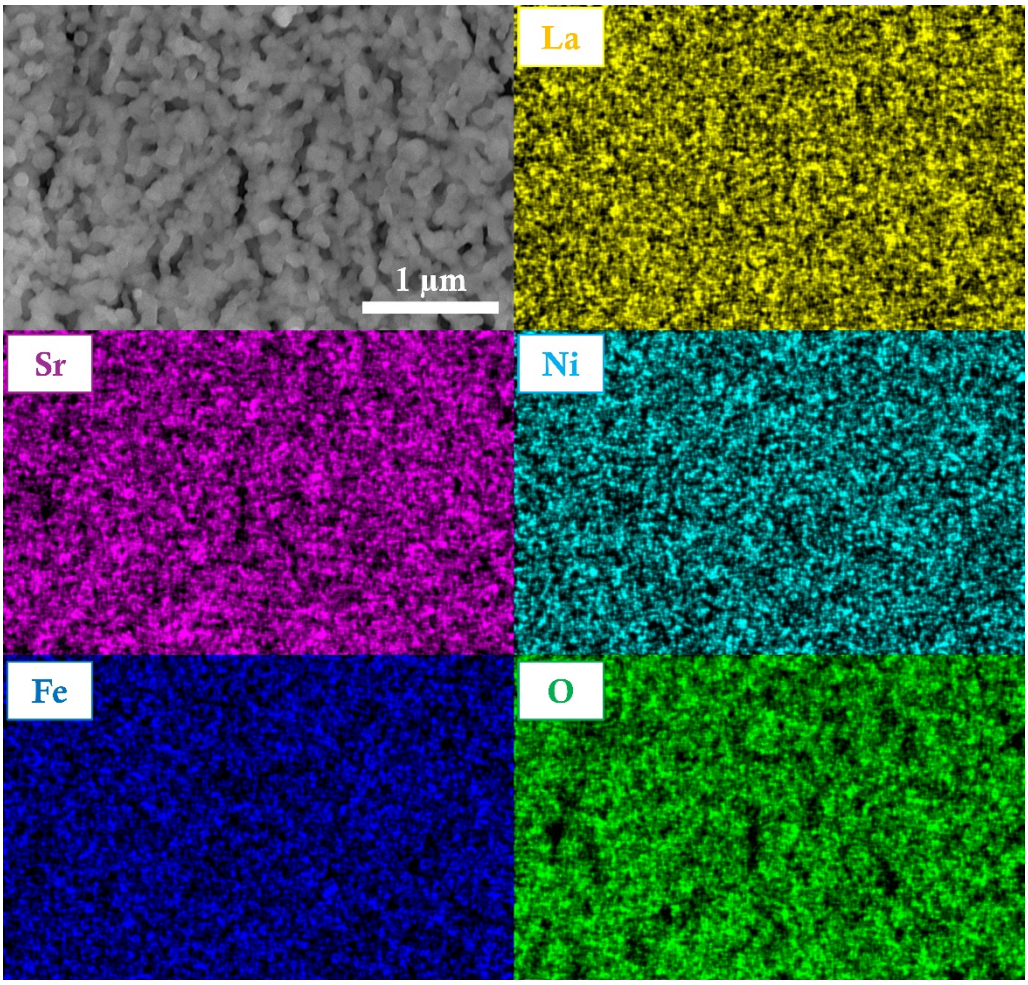

Figure S4. SEM-EDS mapping of LSNF.

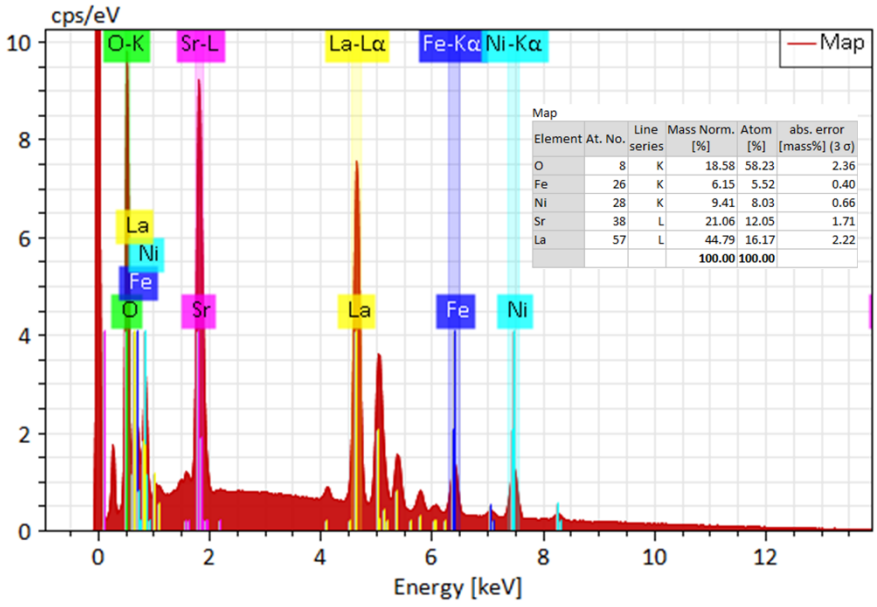

Figure S5. Proportion of each element in LSNF.

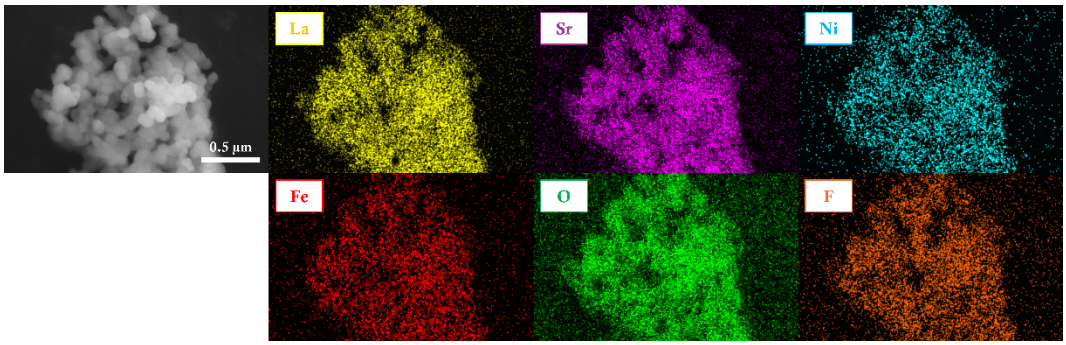

Figure S6. SEM-EDS mapping of LSNF-F.

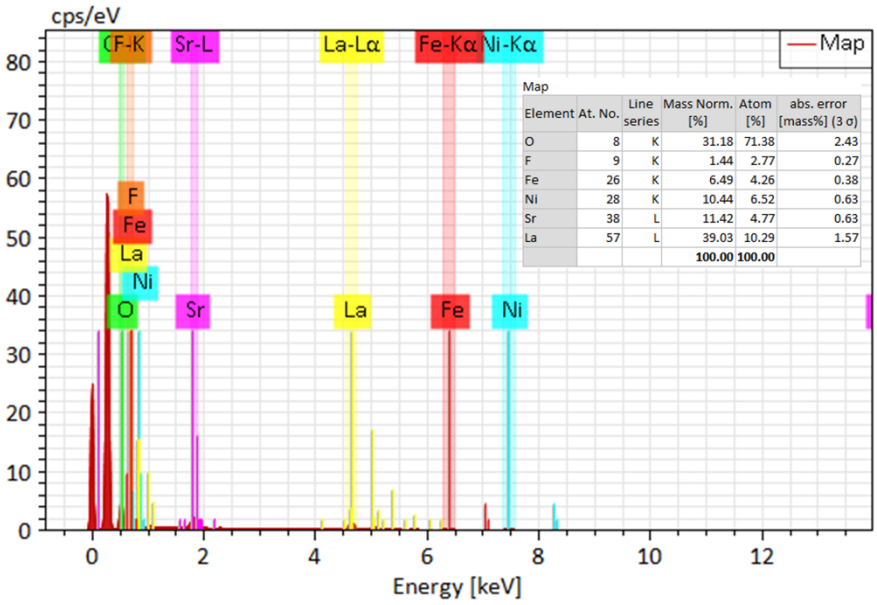

Figure S7. Proportion of each element in LSNF-F.

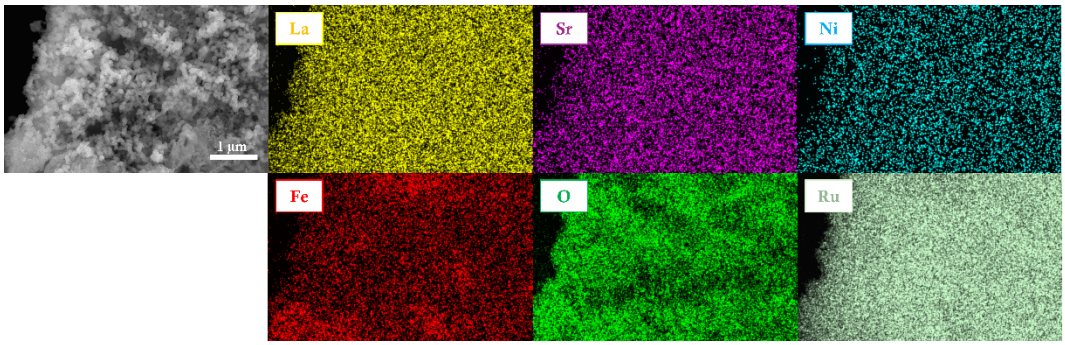

Figure S8. SEM-EDS mapping of RuO_x@LSNF.

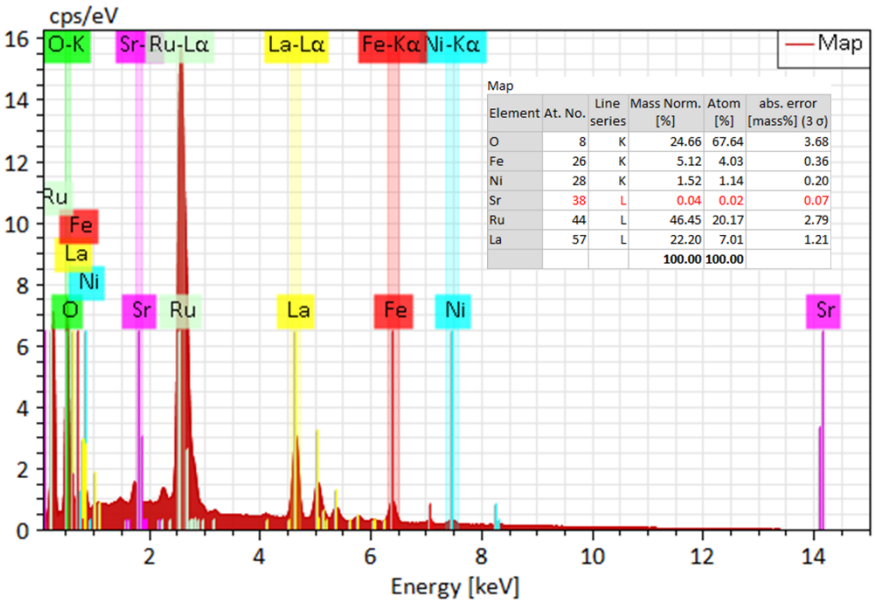

Figure S9. Proportion of each element in RuO_x@LSNF.

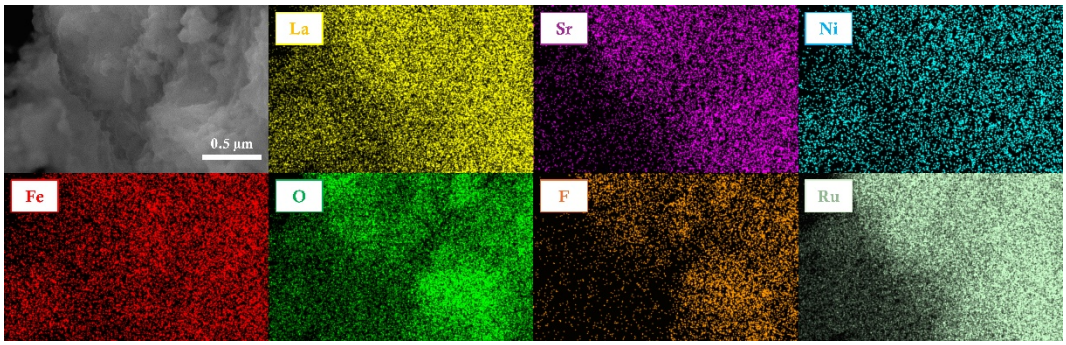

Figure S10. SEM-EDS mapping of RuO_x@LSNF-F.

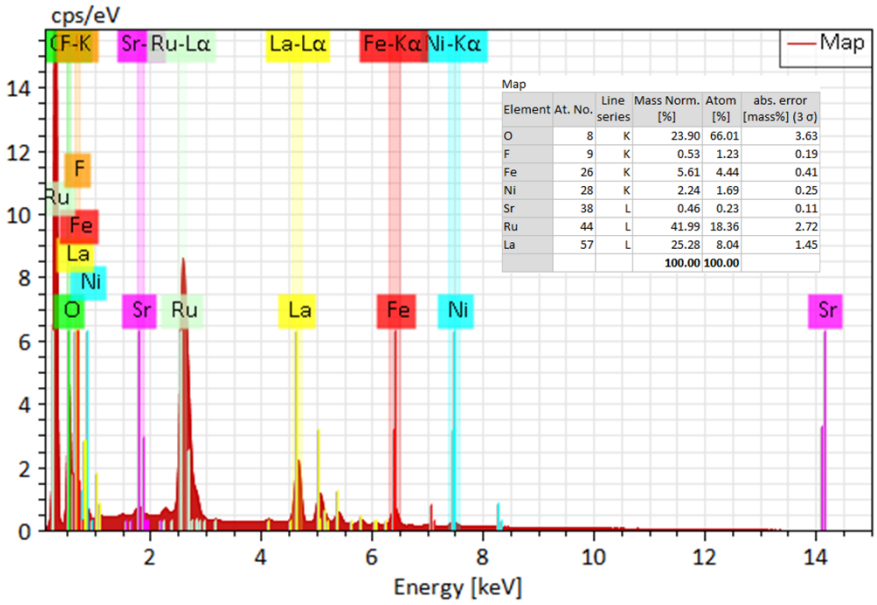

Figure S11. Proportion of each element in RuO_x@LSNF-F.

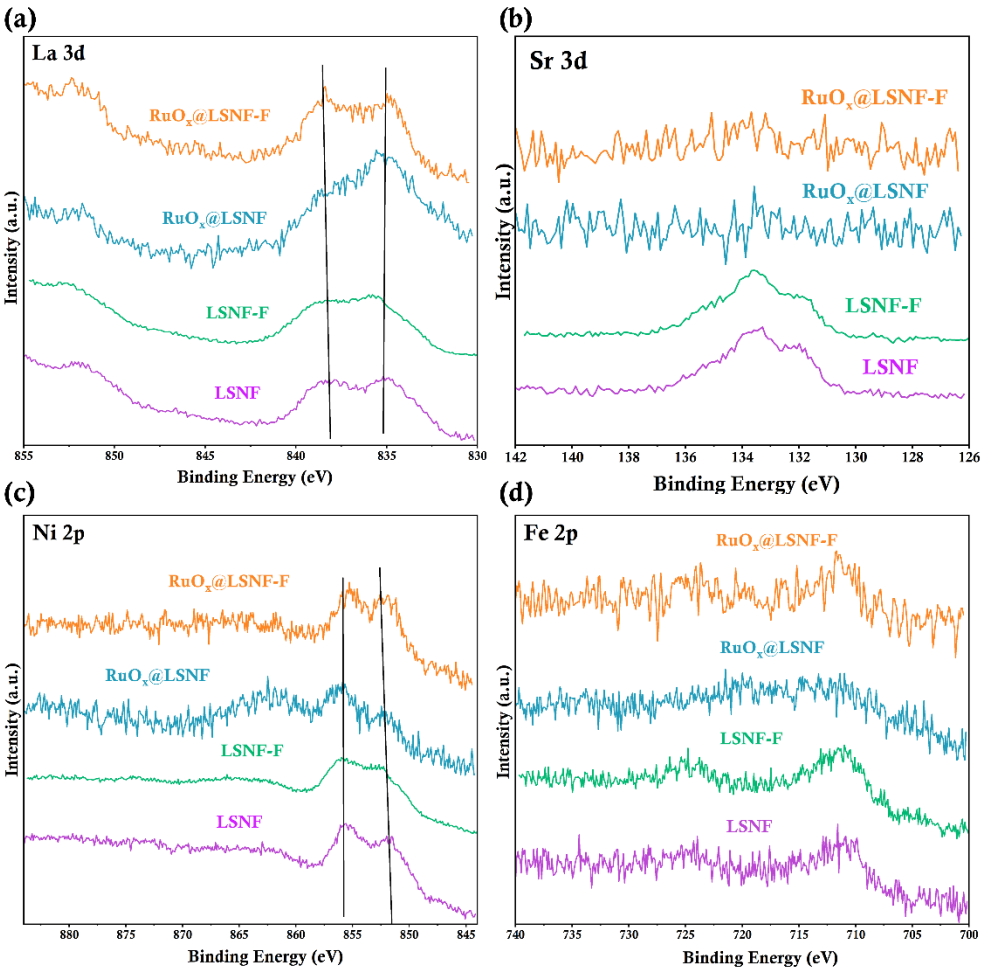

Figure S12. (a) La 3d; (b) Sr 3d; (c) Ni 2p; (d) Fe 2p XPS survey spectra of LSNF, LSNF-F, RuOx@LSNF, RuO$_x$@LSNF-F.

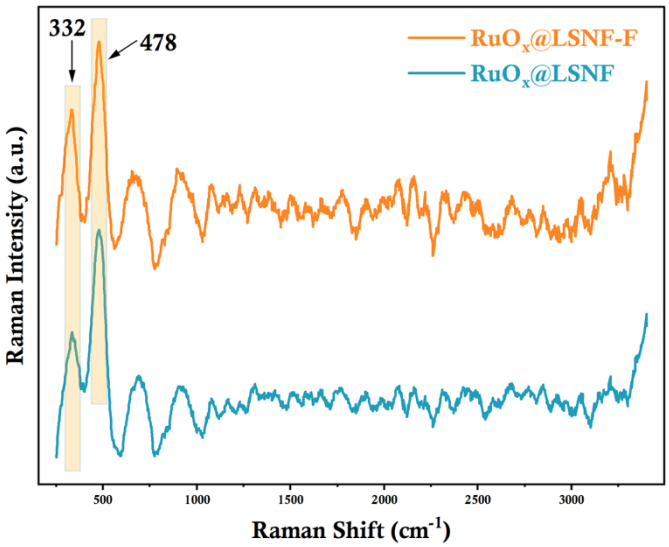

Figure S13. Raman shifts of RuO_x@LSNF-F and RuO_x@LSNF.

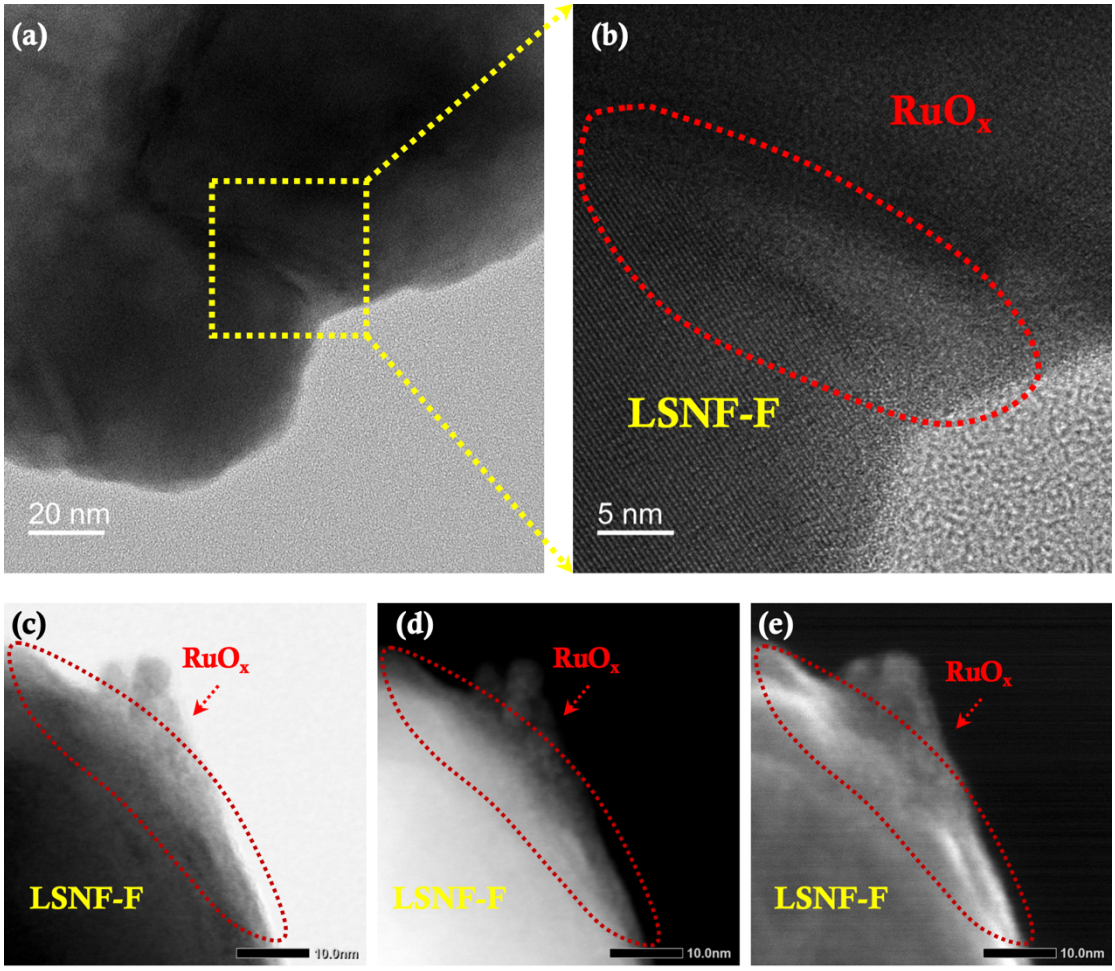

Figure S14. Structural characterization of RuO_x@LSNF-F. (a) Low-magnification HRTEM image of RuO_x@LSNF-F, showing the overall morphology of the catalyst with a uniform particle size. (b) High-magnification HRTEM image of the region marked by the yellow dashed box in (a), clearly revealing a distinct core-shell structure: the inner crystalline LSNF-F support with well-ordered lattice fringes, and the outer amorphous RuO_x layer with no observable lattice fringes, confirming the successful loading of amorphous RuO_x on the perovskite support. (c)-(e) HAADF-STEM images of RuO_x@LSNF-F at different magnifications, further verifying the uniform distribution of the amorphous RuO_x overlayer on the surface of the crystalline LSNF-F support.

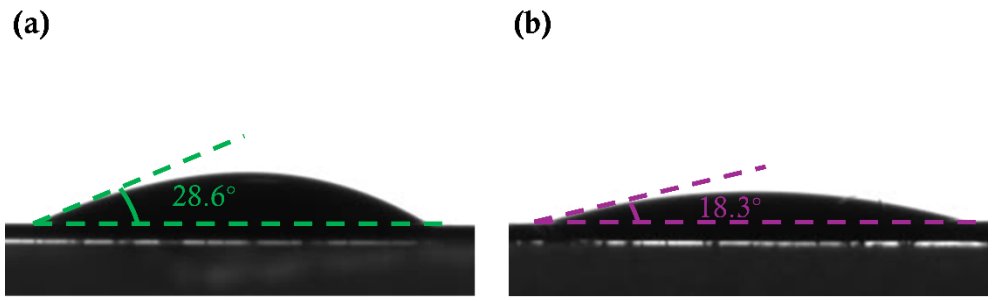

Figure S15. Water contact angle of (a) LSNF-F; (b) LSNF.

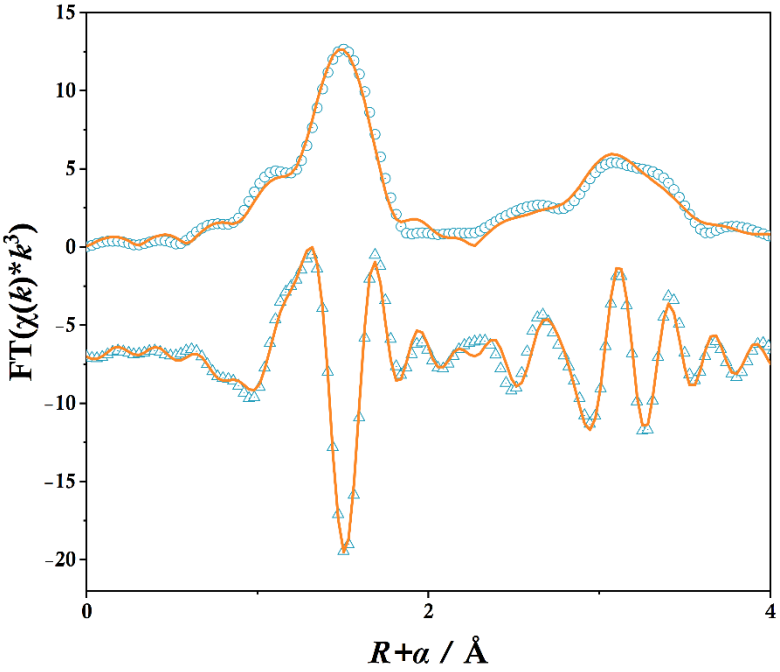

Figure S16. Ru K-edge EXAFS (points) and curvefit (line) for RuO_x@LSNF-F, shown in R-space (FT magnitude and imaginary component). The data are k^3-weighted and not phase-corrected.

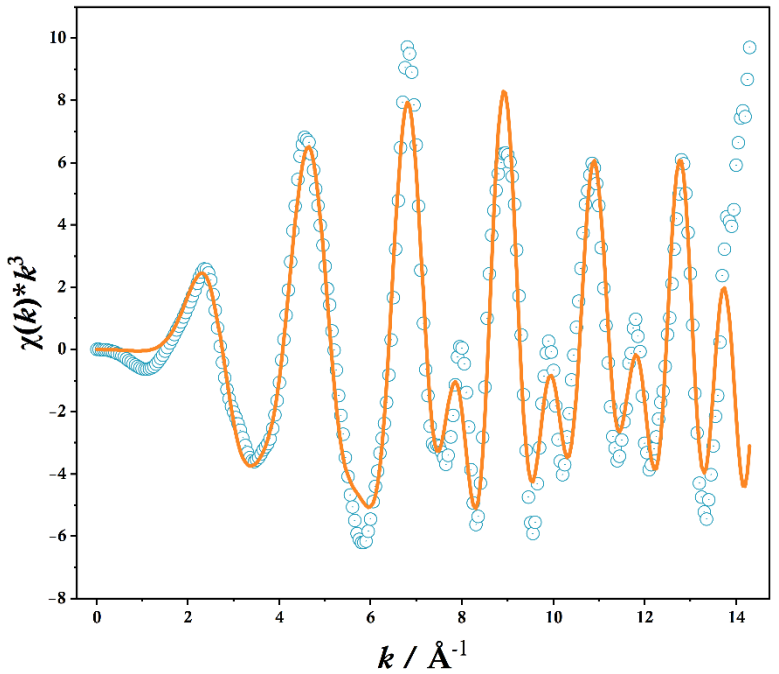

Figure S17. Ru K-edge EXAFS (points) and the curvefit (line) for RuO_x@LSNF-F, shown in k^3-weighted K-space.

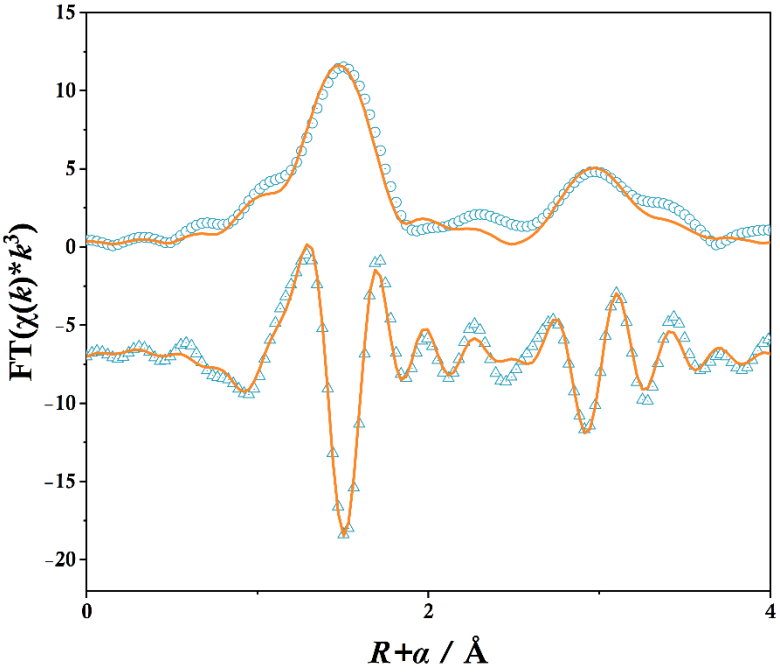

Figure S18. Ru K-edge EXAFS (points) and curvefit (line) for RuO_x@LSNF, shown in R-space (FT magnitude and imaginary component). The data are k^3-weighted and not phase-corrected.

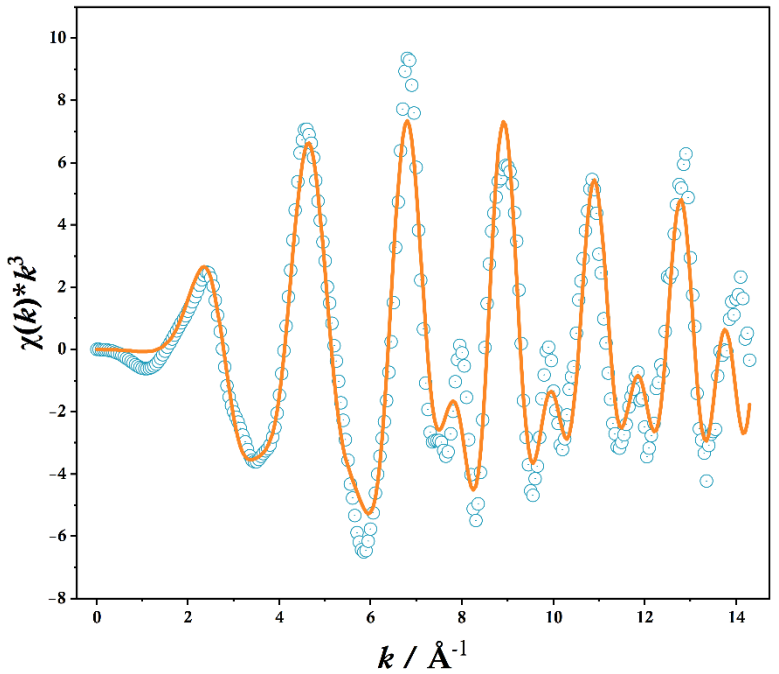

Figure S19. Ru K-edge EXAFS (points) and the curvefit (line) for RuO_x@LSNF, shown in k^3-weighted K-space.

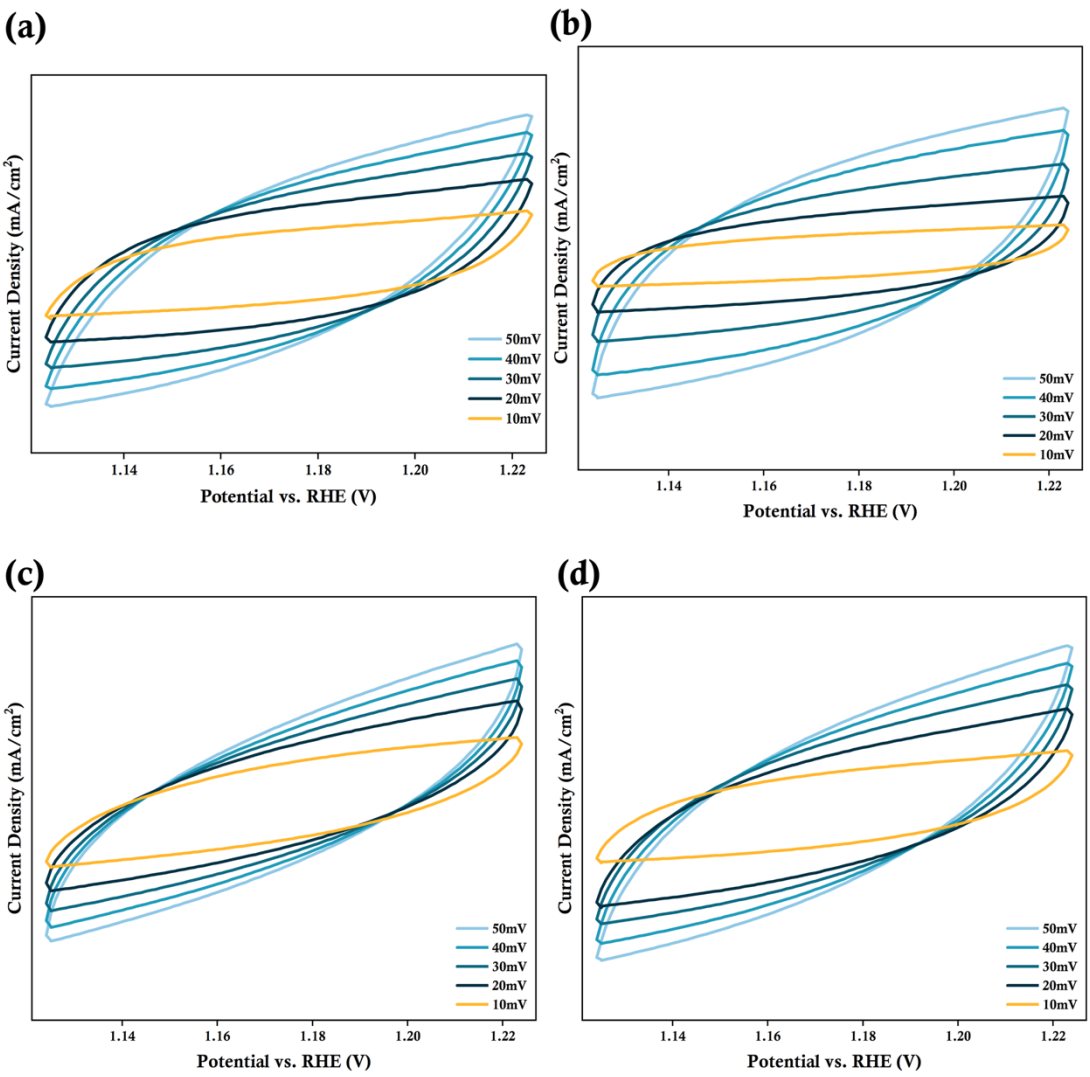

Figure S20. CV curves at different scan rates of (a) RuO_x@LSNF-F; (b) RuO_x@LSNF; (c) LSNF-F; (d) LSNF.

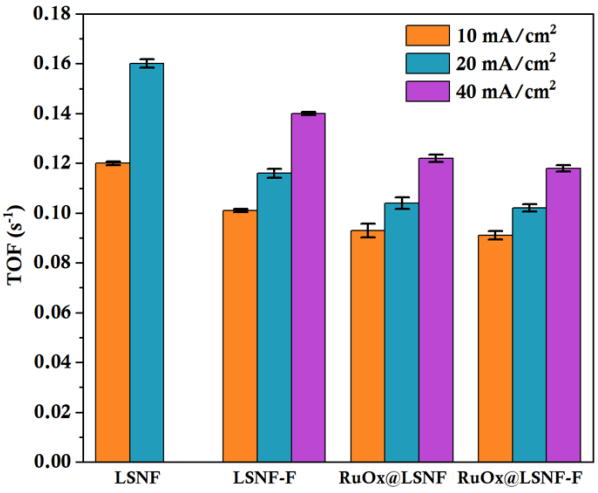

Figure S21. TOF values of the catalysts calculated at a fixed current density of 10/20/40 mA/cm^2 based on the Ru molar amount quantified by ICP-MS. The error bars represent the standard deviation (SD) from three independent measurements.

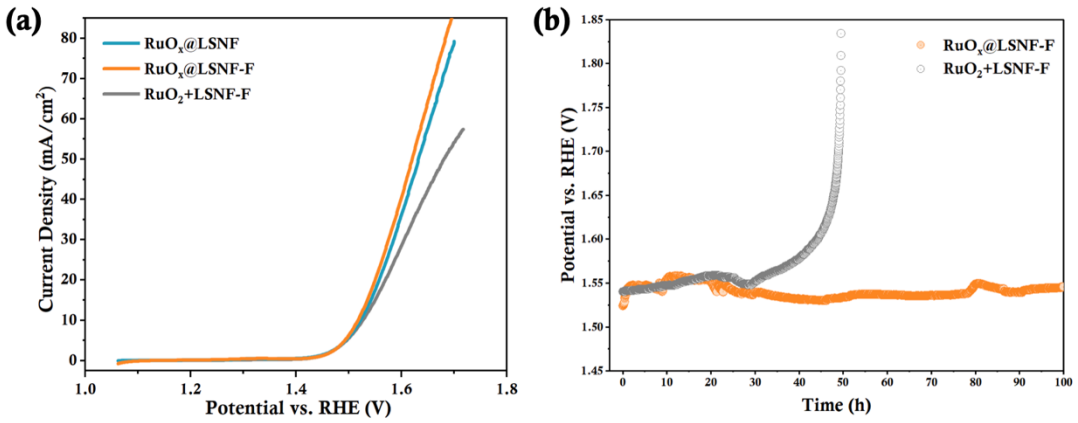

Figure S22. Comparison (a) LSV activity and (b) CP time of RuO_x@LSNF-F, RuO_x@LSNF and RuO_2+LSNF-F.

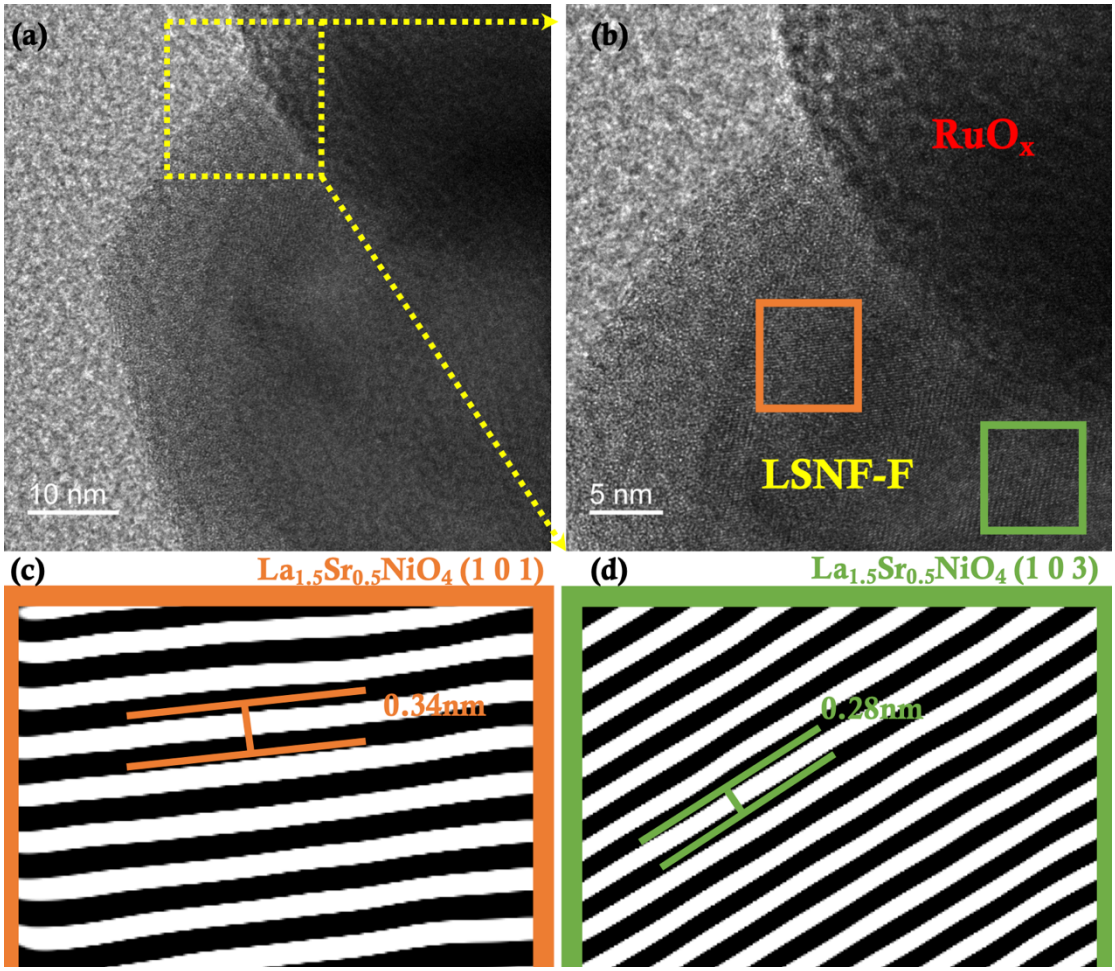

Figure S23. Post-93h-durability (a), (b) HRTEM images and (c), (d) loval inverse FFT images of RuO_x@LSNF-F.

Table S1

ICP-MS test result of RuO_x@LSNF-F.

Ru (wt%)	La (wt%)	Sr (wt%)	Ni (wt%)	Fe (wt%)
31.420	27.585	13.058	10.063	8.596

Table S2

Curvefit parameters[a] for Ru K-edge EXAFS for RuO_x@LSNF-F standard

Path	*d* [b]/ Å	*N*	*R*/ Å	σ^2/Å^2	ΔE/eV	R-factor
Ru – O	1.986	5.3±0.4	1.96±0.01	0.003±0.001	-3.09±0.86	0.017
Ru – Ru1	3.105	6.3±0.8	3.17±0.02	0.002[c]		
Ru – Ru2	3.539	1.1±0.1	3.55±0.01	0.000[c]		

[a] S_0^2 was fixed as 1.0. Data ranges: $2.25 \leq k \leq 13$ Å^{-1} , $1.0 \leq R \leq 3.5$ Å. The number of variable parameters is 8, out of a total of 16.9 independent data points. [b] The distances for Ru – O and Ru – Ru are from the crystal structure of RuO_2. [c] These Debye-Waller factors were constrained as σ^2 (Ru – Ru1) = 0.002 and σ^2 (Ru – Ru2) = 0.000 for reducing the number of variables.

Table S3

Curvefit parameters[a] for Ru K-edge EXAFS for RuO_x@LSNF standard

Path	d [b] / Å	N	R/ Å	σ^2/Å^2	ΔE/eV	R-factor
Ru – O	1.986	5.2±0.5	1.96±0.01	0.003±0.001	-1.97±0.8	0.017
Ru – Ru1	3.105	7.9±0.8	3.19±0.02	0.004 [c]		
Ru – Ru2	3.539	1.3±0.2	3.55±0.03	0.000 [c]		

[a] S_0^2 was fixed as 1.0. Data ranges: $2.25 \leq k \leq 12$ Å^{-1} , $1.0 \leq R \leq 3.2$ Å. The number of variable parameters is 8, out of a total of 13.45 independent data points. [b] The distances for Ru – O and Ru – Ru are from the crystal structure of RuO_2. [c] These Debye-Waller factors were constrained as σ^2 (Ru – Ru1) = 0.004 and σ^2 (Ru – Ru2) = 0.000 for reducing the number of variables

Table S4

Dissolution of RuO_x@LSNF-F in 1M KOH after 100 h CP test (results from ICP-MS test for 80ml sample used for CP test) and the percentage of dissolved fraction to its original mass (fresh 1M KOH electrolyte has been confirmed by ICP-MS test to be free of La, Sr, Ni, Fe and Ru).

	La	Sr	Ni	Fe	Ru
Concentration of metal elements in the electrolyte (mg/L)	0.001	0.002	0.033	0.002	0.003
Percentage of dissolved fraction	0.58%	2.45%	52.41%	3.72%	1.52%

Table S5

Comparison of overpotentials and CP test hours @ 10mA/cm^2 of reported Ru-based and perovskite-based catalysts in alkaline media.

	Electrolyte	Overpotential @ 10mA/cm^2 (mV)	CP test hours (h)	Reference
RuO_x@LSNF-F	1M KOH	287	100	This work
RuO_x@LSNF	1M KOH	292	33	This work
LSNF-F	1M KOH	317	15	This work
Mn/Ru DSA	1M NaOH	300	14.5	(1)
RuO_2 com.	1M KOH	366	10	(2)
Ru_2Ni_2 SNs/C	1M KOH	310	40	(3)
SFR30	1M KOH	334	96	(4)
$Ni_{1.25}Ru_{0.75}P$	1M KOH	340	20	(5)
PSCR0.05	0.1M KOH	321	10	(6)
SNCF-NR	0.1M KOH	390	10	(7)
LSCF-30	1M KOH	360	56	(8)

r-LSCN-P	0.1M KOH	410	14	(9)
SCFM10	1M KOH	310	100	(10)

References

(1) Browne, M. P.; Nolan, H.; Duesberg, G. S.; Colavita, P. E.; Lyons, M. E. G. Low-Overpotential High-Activity Mixed Manganese and Ruthenium Oxide Electrocatalysts for Oxygen Evolution Reaction in Alkaline Media. *ACS Catalysis* **2016**, *6* (4), 2408–2415. https://doi.org/10.1021/acscatal.5b02069.

(2) Gao, M.-R.; Cao, X.; Gao, Q.; Xu, Y.-F.; Zheng, Y.-R.; Jiang, J.; Yu, S.-H. Nitrogen-Doped Graphene Supported $CoSe_2$ Nanobelt Composite Catalyst for Efficient Water Oxidation. *ACS Nano* **2014**, *8* (4), 3970–3978. https://doi.org/10.1021/nn500880v.

(3) Ding, J.; Shao, Q.; Feng, Y.; Huang, X. Ruthenium-Nickel Sandwiched Nanoplates for Efficient Water Splitting Electrocatalysis. *Nano Energy* **2018**, *47*, 1–7. https://doi.org/10.1016/j.nanoen.2018.02.017.

(4) Zhang, W.; Xue, M.; Zhang, X.; Si, C.; Tai, C.; Lu, Q.; Wei, M.; Han, X.; Ma, J.; Chen, S.; Guo, E. Boosting Oxygen/Hydrogen Evolution Catalysis via Ruthenium Doping in Perovskite Oxide for Efficient Alkaline Water Splitting. *Applied Surface Science* **2024**, *664*, 160278. https://doi.org/10.1016/j.apsusc.2024.160278.

(5) Liyanage, D. R.; Li, D.; Cheek, Q. B.; Baydoun, H.; Brock, S. L. Synthesis and Oxygen Evolution Reaction (OER) Catalytic Performance of $Ni_{2-x}Ru_xP$ Nanocrystals: Enhancing Activity by Dilution of the Noble Metal. *Journal of Materials Chemistry A* **2017**, *5* (33), 17609–17618. https://doi.org/10.1039/c7ta05353c.

(6) Zhao, Y.-N.; Liu, C.; Xu, S.; Min, S.; Wang, W.; Mitsuzaki, N.; Chen, Z. A/B-Site Management Strategy to Boost Electrocatalytic Overall Water Splitting on Perovskite Oxides in an Alkaline Medium. *Inorganic Chemistry* **2023**, *62* (31), 12590–12599. https://doi.org/10.1021/acs.inorgchem.3c01965.

(7) Zhu, Y.; Zhou, W.; Zhong, Y.; Zhong, Q.; Chen, X.; Liu, M.; Zhou, W. A Perovskite Nanorod as Bifunctional Electrocatalyst for Overall Water Splitting. *Advanced Energy Materials* **2017**, *7* (8), 1602122–1602122. https://doi.org/10.1002/aenm.201602122.

(8) Zong, R.; Fang, Y.; Zhu, C.; Zhang, X.; Wu, L.; Hou, X.; Tao, Y.; Shao, J. Surface Defect Engineering on Perovskite Oxides as Efficient Bifunctional Electrocatalysts for Water Splitting. *ACS Applied Materials & Interfaces* **2021**, *13* (36), 42852–42860. https://doi.org/10.1021/acsami.1c11895.

(9) Wang, Y.; Wang, Z.; Jin, C.; Li, C.; Li, X.; Li, Y.; Yang, R.; Liu, M. Enhanced Overall Water Electrolysis on a Bifunctional Perovskite Oxide through Interfacial Engineering. *Electrochimica Acta* **2019**, *318*, 120–129. https://doi.org/10.1016/j.electacta.2019.06.073.

(10) Zhang, W.; Si, C.; Lu, Q.; Wei, M.; Han, X.; Chen, S.; Guo, E. Mo-Doped SrCo0.5Fe0.5O3-δ Perovskite Oxides as Bifunctional Electrocatalysts for Highly Efficient Overall Water Splitting. *Electrochimica Acta* **2024**, *491*, 144323. https://doi.org/10.1016/j.electacta.2024.144323.